Materials Science & Engineering A 859 (2022) 144189

Contents lists available at ScienceDirect

Materials Science & Engineering A

journal homepage: www.elsevier.com/locate/msea

The effects of microstructure on deformation twinning in Mg WE43

Zhe Chen [a,b,*], Mohammadreza Yaghoobi [b], Veera Sundararaghavan [c], John Allison [b], Samantha Daly [a]

[a] Department of Mechanical Engineering, University of California Santa Barbara, Santa Barbara, CA, 93106, USA
[b] Department of Materials Science & Engineering, University of Michigan, Ann Arbor, MI, 48109, USA
[c] Department of Aerospace Engineering, University of Michigan, Ann Arbor, MI, 48109, USA

ARTICLE INFO

Keywords:
Twinning
Digital image correlation
Crystal plasticity
Deformation
Magnesium

ABSTRACT

The interplay between microstructure and deformation twinning in a WE43-T6 Mg alloy under uniaxial compression was investigated using a combination of scanning electron microscopy with digital image correlation (SEM-DIC) and crystal plasticity finite element (CPFE) simulation. To improve understanding of the statistical characteristics of deformation twin formation, microstructural effects were characterized in over 1000 grains through metrics including the nominal Schmid Factor, grain size, geometric compatibility factor (m'), residual Burgers vector, and the strain accommodated by neighboring grains. There was a strong correlation between the nominal Schmid Factor and both twin activation and variant selection, but this was not fully deterministic. Deformation twinning also exhibited a strong dependence on existing slip and twinning in the neighboring grain and on the m' value. Within the range of grain sizes present in this condition, grain size was determined to have minimal effect on deformation twinning. Statistical analysis of CPFE simulations was used to further investigate microstructural effects on twinning, and qualitatively captured the effect of the nominal Schmid Factor.

1. Introduction

Magnesium (Mg) alloys are of interest for lightweight structural applications, including automobiles, aerospace, aircraft, and biomedical devices [1,2]. To accelerate the development and application of Mg alloys, work is needed to better understand their deformation behavior, particularly their strengthening and failure mechanisms. Twinning is an important mode of deformation in hexagonal close-packed materials such as Mg. For Mg and its alloys, basal slip exhibits a much lower critical resolved shear stress (CRSS) than all other slip modes, and twinning plays an important role in accommodating deformation along the c-axis. It significantly affects the material and mechanical properties of Mg, including its crystallographic texture, tension-compression anisotropy, and formability. An improved understanding of twinning activity, including twin nucleation, variant selection, and twin growth, is a key component in the accurate modeling of Mg alloys and in their targeted design for desired properties.

The nucleation of deformation twinning has been modeled as a process that requires twinning partials from the dissociation of pre-existing dislocations [3–8]. Grain boundaries are preferential sites for twin nucleation, as they are sources for high densities of dislocations, can support the complex rearrangement to form stable twin nuclei, and are favorable locations for stress concentrations that drive these reactions [9]. The nucleation and growth of deformation twinning in Mg are influenced by factors including the driving force in the parent grain and the constraints and stimuli imposed by the neighboring grains.

An important criterion for twin activation is the nominal twin Schmid Factor (SF) in individual grains. The nominal SF indicates the extent of the external stress field as defined by assuming a uniaxial stress in a specific sample direction and resolving this onto the twinning plane in the twinning shear direction in each individual grain. The nominal SF does not take into account the influence of the strain from neighboring grains, which may result in an actual SF different than the nominal. Throughout this paper, the term Schmid Factor (SF) denotes the nominal Schmid Factor unless otherwise noted. Many studies have observed strong correlations between twin activation and/or twin variant selection with SF, or related concepts such as the rank of the SF or the 'normalized' SF (e.g. the SF of a twin variant normalized by the highest possible SF among all crystallographically equivalent variants) [10–16]. In general, twins with a high twin SF are more likely to activate, and

* Corresponding author. Department of Mechanical Engineering, University of California Santa Barbara, Santa Barbara, CA, 93106, USA.
E-mail address: chenzhe@ucsb.edu (Z. Chen).

https://doi.org/10.1016/j.msea.2022.144189
Received 30 May 2022; Received in revised form 3 October 2022; Accepted 12 October 2022
Available online 17 October 2022

most active twin variants exhibit a high SF. However, active variants are not always those with the highest SF, and likewise, high SF variants do not always exhibit twinning.

The effect of strain accommodation on twin nucleation has been proposed in a series of prior works [11–13,17]. The primary idea is that twin nucleation requires strain accommodation in the neighboring matrix, and the ease of such strain accommodation can affect twin variant selection. These analyses were based on transforming the shear or displacement gradient tensor of a given twin system into the crystal coordinate system of a neighboring grain, and then correlating the transformed value with the extent of activity required for different deformation modes in the neighboring grain. The models provided reasonable explanation for twin nucleation and variant selection in several conditions, e.g., for both extension and contraction twins, for primary, secondary, and tertiary twins, in AM30 and AZ31 alloys [11–13,17]. However, there exists disagreement in the literature on this mechanism, where some studies have found that the strain accommodation models do not accurately predict twin variant formation [15,18]. Alternate effects, such as the stimulation from slip activity in neighboring grains [15] and the interaction among twin variants [18] have been proposed as more important for twin nucleation and variant selection.

To evaluate the effect of grain boundaries and neighbor grains on twin activity, metrics that describe the geometric alignment of the lattice or slip/twin systems across the grain boundary have been considered. These include the geometric compatibility factor (m'), the residual Burgers vector, and the grain boundary misorientation, etc. The m' factor, originally defined by Luster and Morris [19] to describe the alignment of slip systems, was later extended to the analysis of both slip and twinning [20]. A high value of m' represents good alignment of both the slip/twin planes and the slip/twin directions. Some investigations found that the stimulation from basal slip in a neighboring grain with a high m' factor can induce twinning [14,15], but counter evidence also existed where the correlation between twinning and m' factor was not observed [17]. The residual Burgers vector only considers relationship between the slip/twin directions and is more often used to analyze slip transfer [21]. The grain boundary misorientation does not explicitly measure the alignment of slip/twin planes or directions, but some studies have shown that twinning was preferred at low misorientation grain boundaries [10].

Crystal plasticity is a useful means to capture the mechanical response of Mg alloys [22–33]. Crystal plasticity models have successfully captured the macroscale response of Mg alloys, including its anisotropy under varied loading conditions due to twinning. Crystal plasticity models have been combined with microscale deformation information from both SEM-DIC and synchrotron X-ray diffraction experiments to examine the deformation mechanisms present in Mg alloys [34–41]. Abdolvand et al. [34] addressed deformation twinning in an AZ31B Mg alloy using data from synchrotron X-ray diffraction experiments combined with CPFE simulation. Greeley et al. [35] captured the evolution of slip and twinning mechanisms in an Mg–Nd alloy using the HEDM and CPFE. Githens et al. [36] calibrated a crystal plasticity model for the Mg alloy WE43 using SEM-DIC experimental data and compared the results of full-field CPFE simulation with experiment. They showed that if the material model properties are calibrated appropriately, CPFE can capture the slip and twinning patterns observed in experiment. Ganesan et al. [37] incorporated an integrated framework of SEM-DIC with CPFE to capture the effects of heat treatment on the response of WE43 Mg. They compared both the stress-strain response and slip activities of T5 and T6 tempers, and showed that simulation is an essential part of the framework to unravel the effect of heat treatments on the underlying deformation mechanisms. Yaghoobi et al. [38] presented a framework to calibrate and validate the CPFE simulation of extension twinning using the SEM-DIC experimental data for WE43-T6.

As introduced above, although many studies have been performed to investigate the effect of different microstructure descriptors/metrics on twinning activity, there exist contradictory findings. Many conclusions were based on a limited number of observations, and their general applicability remain to be investigated. One motivation of the current study is to evaluate the effect of microstructure features on twinning based on statistically significant number of observations. In addition, although strain accommodation models [11–13,17] provide reasonable explanations to a number of observations, none of the studies directly measured the experimental strain field. Therefore, another motivation of the current study is to take advantage of the full-field strain measurement capability of digital image correlation to analyze the correlation between strain distribution and twinning activation. The experimental procedures for *in-situ* SEM-DIC compression tests performed on a WE43 Mg alloy were previously reported by the authors [37,38]. In the current investigation, the relationship between microstructural features and twin activation and variant selection was analyzed in over 1500 grains in the WE43-T6 Mg alloy. Different microstructural criteria were analyzed including the SF, grain size, grain boundary, neighboring grains, m' factor, residual Burgers vector, and strain accommodation by neighboring grains. A multi-scale rate--independent crystal plasticity model, developed and calibrated for WE43-T6 by Yaghoobi et al. [24,38], was used to further investigate the effect of microstructure on deformation twinning. The multi-scale crystal plasticity model was implemented in the open source PRISMS-Plasticity CPFE software [39]. While in the previous work on WE43 [38], the CPFE framework was calibrated using macroscopic stress-strain and twin content, the focus of the current simulation is to evaluate the twin statistics in WE43 alloy provided by the SEM-DIC experiment.

2. Materials and experiment

The material and experimental details are reported in previous work by the authors [38,40] and are briefly described as follows. A rare earth containing Mg alloy WE43 in the T6 condition was received from Magnesium Elektron Ltd as a hot rolled plate in the T5 condition, solution treated at 525 °C for 8 h, water quenched, and peaked-aged at 250 °C for 16 h to reach the T6 condition. The nominal composition of the alloy in wt.% is 3.74 Y, 2.10 Nd, 0.52 Gd, 0.45 Zr, 0.016 Zn, and Mg in balance. A dogbone-shaped test specimen with a gage dimensions of 10 mm long, 3.5 mm wide, and 3.5 mm thick was cut using electrical discharge machining with the loading direction along the rolling direction (RD), and sample normal direction (ND) along the normal direction of the plate. The specimen was polished and etched using standard metallographic techniques and characterized by electron backscatter diffraction (EBSD).

The sample surface was patterned with 300 nm diameter gold nanoparticles for deformation tracking, following the method of [41,42]. In-situ compression testing was performed inside a FEI Teneo scanning electron microscope (SEM) using a Kammrath & Weiss thermo-mechanical testing stage, with a nominal strain rate of $10^{-4}\,s^{-1}$. The test was paused at global strain levels of $\varepsilon^{G} = -0.003$, -0.004, -0.012, -0.023, and -0.039 to capture secondary electron images using a custom automated system for multi-tile imaging [43] for a sample area of 5.7 mm × 3.4 mm with 88 nm/pixel resolution. DIC was performed using a commercial software Vic2D 6 (Correlated Solutions, Inc., Irmo, SC) with a subset size of 21 pixels and step size of 5 pixels to extract displacements and Lagrangian strain fields.

3. Results

3.1. Microstructure

The microstructure and texture of the sample are shown in Fig. 1. The sample contained equiaxed grains. The average grain diameter, calculated from EBSD using 5° tolerance angle and area weighted method, was 116 μm [38]. The material exhibited a moderately weak

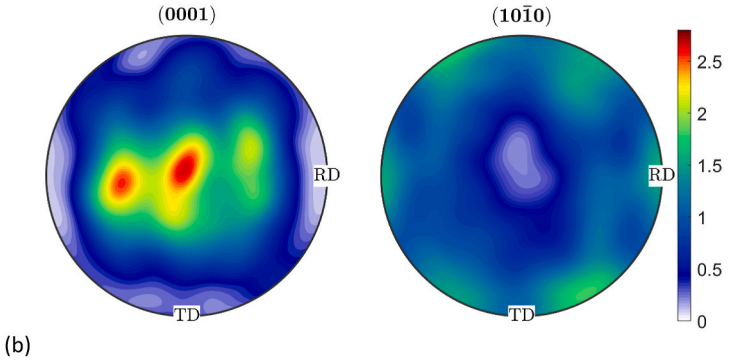

Fig. 1. (a) EBSD inverse pole figure map of the sample normal direction. Reprinted from Materials Science and Engineering A, vol. 736, Z. Chen, S. Daly, Deformation twin identification in magnesium through clustering and computer vision, 61–75, (2018), with permission from Elsevier. (b) Basal and prismatic pole figures of the WE43-T6 sample. Reprinted by permission from Springer Nature Customer Service Center GmbH: Springer, Integrating Materials and Manufacturing Innovation, Crystal Plasticity Finite Element Modeling of Extension Twinning in WE43 Mg Alloys: Calibration and Validation, M. Yaghoobi et al. (2021).

texture, where the basal poles exhibited the highest intensity around the sample normal direction (ND), and there was a slight split of the basal poles towards the rolling direction (RD). A slight six-fold symmetry was observed on the prismatic pole figure. Orientations that favor either basal slip or extension twinning were found in a large percentage of grains.

3.2. Deformation twin variant identification

Twinning variants were identified via physics-based clustering and computer vision (for more details on this identification process, please see Refs. [38,40]). The intersection of twinning and grain boundaries was manually identified from axial strain (ε_{xx}) and twin variant maps at multiple global strain levels. Fig. 2 shows an example of a twin variant map at $\varepsilon^G = -0.023$, with twin variants marked by different colors. The inset shows the axial strain map and the twin variant map at high magnification. The six variants of the $\{10\bar{1}2\}\langle\bar{1}011\rangle$ type extension twinning were considered. Most twinned grains contained one or two twin variants: among the 1515 grains in the sample area, 357 (~23%) grains had twinned prior to a global strain of $\varepsilon^G = -0.039$. 154 grains exhibited one variant, 199 grains exhibited two variants, and 4 grains exhibited three variants.

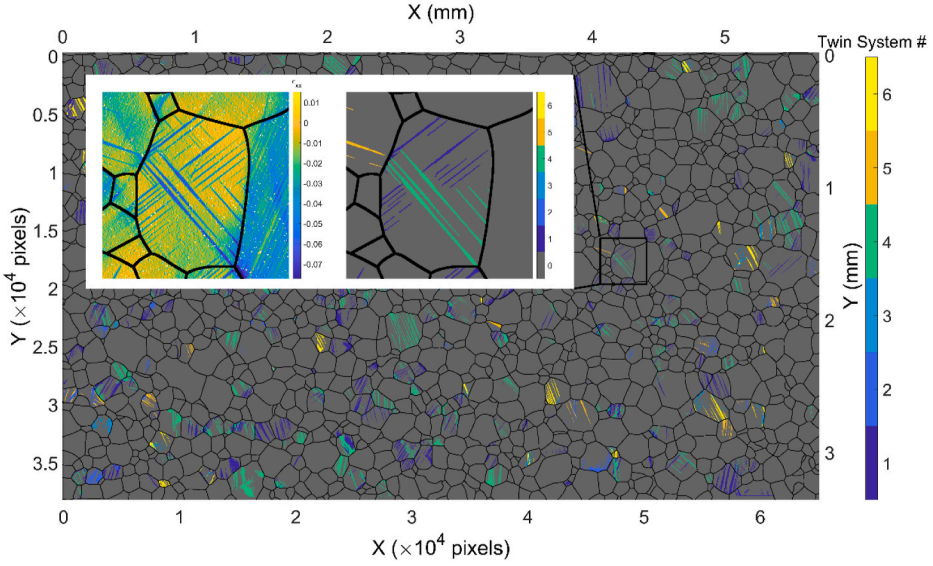

Fig. 2. Twin variant map at $\varepsilon^G = -0.023$. The six variants of the $\{10\bar{1}2\}\langle\bar{1}011\rangle$ type extension twinning were considered. Different variants are marked by different colors. The inset provides a magnified view of the axial strain map (left) and twin variant map (right) of a local microstructure.

3.3. Effect of grain features on twinning

3.3.1. Effect of Schmid Factor

Consistent with previous studies, Schmid Factor (SF) significantly influenced the activation of twin variants in WE43, but was not a singularly deterministic factor. A representative example is shown in Fig. 3(a), which summarizes the number of potential twin variants that were twinned (red) and not twinned (blue) versus their SF at $\varepsilon^G = -0.039$. All six possible extension twin variants in each grain were considered, but only those with positive SF were summarized. The overall twin area fraction measured on the surface was 8.7% ± 0.51%, and the percentage of twin variants active was larger in grains with larger SFs. However, even across all grains with a SF > 0.45, only ~60% of variants twinned, as shown in Fig. 3(a).

Most grains with a high basal SF did not twin. Fig. 3(b) summarizes the number of grains twinned (red) and not twinned (blue) versus the maximum basal SF of the grain at $\varepsilon^G = -0.039$. A maximum nominal basal (twin) SF is the maximum nominal SF among the three basal (six twin) systems. The observations are consistent with the literature, i.e., that twins are not necessarily observed at all variants that have high values of twin SF, and that not all twinned variants have a high twin SF [10]. As expected, twins with a higher SF were more likely to twin, and twins in a grain with a high maximum nominal basal SF were unlikely to twin.

Twin variants with a relatively high nominal twin SF tended to comprise a larger area fraction of their parent grain, and the area fractions of high twin SF grains exhibited a larger scatter. Fig. 4 summarizes the distribution of the active twin variant sizes represented as the area fraction of their parent grain by box plots, where active twin variants were grouped by their nominal SF at a globally applied uniaxial compressive strain of $\varepsilon^G = -0.039$. The number of observations in each group is indicated by the text in the parentheses above the bottom axis. For each box, the central bar indicates the median, the bottom and top edges indicate the 1st and 3rd quartiles (Q1 and Q3), and the whiskers extend to the most extreme data points that are not considered outliers (where outliers are data points less than Q1 − 1.5 × (Q3-Q1) or greater than Q3 + 1.5 × (Q3-Q1)). The notches, placed at 1.57 × (Q3-Q1)/ $\sqrt{n}$ above and below the median (light blue shaded regions in each box in Fig. 4), where n is the number of observations, provide an approximate measure of the significance of the difference between the medians of different bins. If the notches of two boxes do not overlap, the medians are considered significantly different at a ~95% confidence level. The twin area fractions for groups with SF > 0.4 were, with statistical significance, larger than for those with SF < 0.3 (Fig. 4). Although a small number of low SF twins were also activated, they generally accounted for less than 20% of the parent grain.

The WE43 Mg investigated here exhibited a weak basal texture in the rolling plane and had a large number of grains oriented to favor basal slip. Basal slip was likely the dominant deformation mechanism, especially in untwinned grains, as seen in Fig. 5(a). Fig. 5(a) summarizes the distribution of the grain-averaged effective strain for all untwinned grains at a globally applied uniaxial compressive strain of $\varepsilon^G = -0.039$. The grains were binned by maximum basal SF, and the grain average effective strain was calculated by averaging the effective strain of all data points within that grain. At every data point, the effective strain was calculated by:

$$\varepsilon_{eff} = \sqrt{\frac{2}{3}\left(\varepsilon_{xx}^2 + \varepsilon_{yy}^2 + 2\varepsilon_{xy}^2\right)} \quad \text{Eq. (1)}$$

For grains with a maximum basal SF > 0.2, the effective strain inside the grain increased with increasing maximum basal SF.

A high twin SF encouraged twin activation, but did not necessarily result in a high effective strain inside the grain. This is shown in Fig. 5 (b), which summarizes the distribution of grain averaged effective strain for all twinned grains at $\varepsilon^G = -0.039$, with grains binned by their maximum twin SF. The grain-averaged effective strain exhibited a slight trend of decreasing strain with increasing maximum twin SF, but the

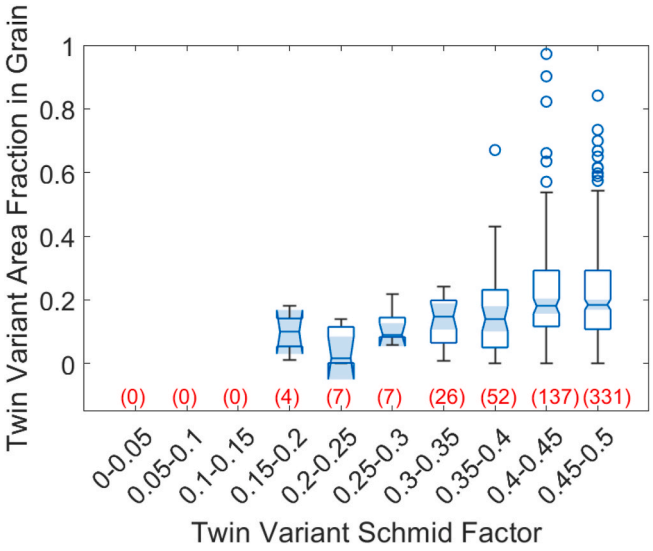

Fig. 4. Box plot summarizing the distribution of the active twin variant size represented as the area fraction of the parent grain, where active twin variants are binned by their nominal SF, at a globally applied strain of $\varepsilon^G = -0.039$. The number of observations in each group is indicated by the red text in the parentheses above the bottom axis. Detailed interpretation of the box plot is provided in the text.

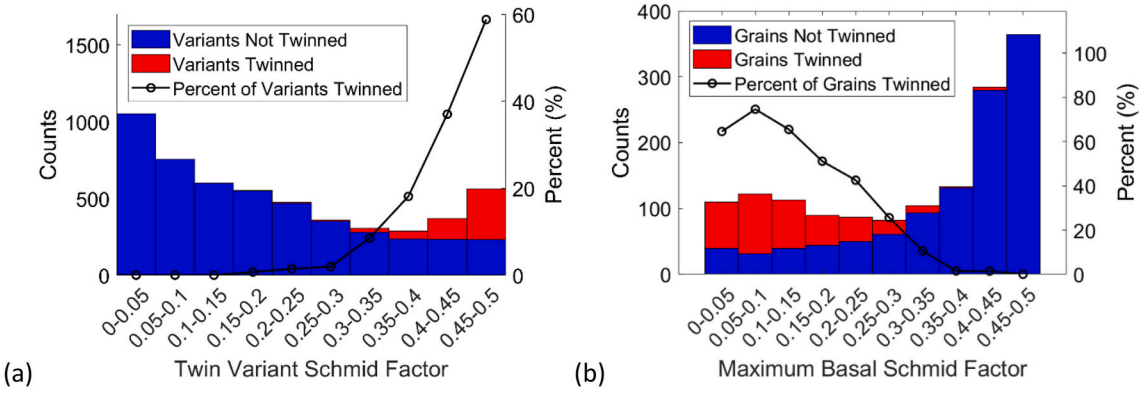

Fig. 3. (a) Number of twin variants twinned (red) and not twinned (blue) vs. their nominal SF at $\varepsilon^G = -0.039$. The percentage of twin variants twinned is plotted using the y-axis on the right. (b) Number of grains twinned (red) and not twinned (blue) vs. their maximum basal SF at $\varepsilon^G = -0.039$.

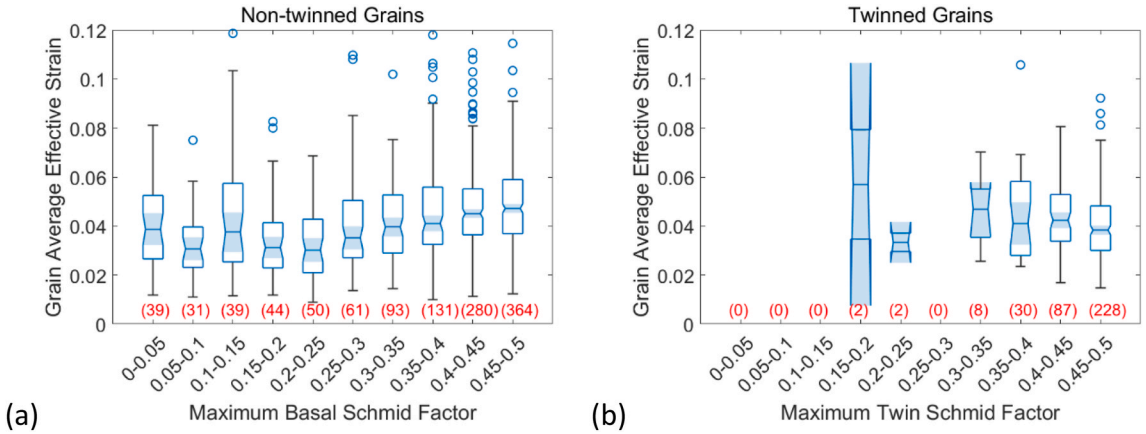

Fig. 5. Boxplot summarizing (a) the distribution of grain-averaged effective strain for all untwinned grains at $\varepsilon^G = -0.039$, with grains binned by their maximum basal SF. For grains with a maximum basal SF > 0.2, the effective strain inside the grain increased with increasing maximum basal SF. (b) Distribution of grain-averaged effective strain for all twinned grains at $\varepsilon^G = -0.039$, with grains binned by their maximum twin SF. The number of observations in each group is indicated by the red text in the parentheses above the x-axis.

difference between groups were not statistically significant based on the overlap of the notches of the boxes. The number of observations in groups with max twin SF < 0.25 were small, and therefore may not provide statistically significant information. It is possible that basal slip also contributed significantly to the strain in the twinned grains, although slip traces were much less evident than twinning on the DIC-obtained strain map. In addition, the effective strain calculation only considered the 2D component of the strain tensor; it is therefore also possible that the high maximum twin SF grains contributed more to the strain in the out-of-plane direction, as this information was not provided by the 2D DIC analysis.

3.3.2. *Effect of grain size*

The nominal grain size of the WE43 was 116 μm with a grain size distribution shown in Fig. 6(a). The number fraction of twinned grains is shown in Fig. 6(b) with grains grouped by diameter (calculated by assuming the grain to be circular). This information was determined at four different globally applied strains. A smaller percentage of the small grains were twinned; however, this could be significantly affected by the fact that the smaller grains contained a larger percentage of noisy data points, which could prevent clear identification of twinning. At $\varepsilon^G = -0.023$ and above, approximately 30% of the grains with a diameter larger than 80 μm were twinned, which is comparable to prior work [10].

Grain size did not appear to affect twin area fraction. Fig. 7

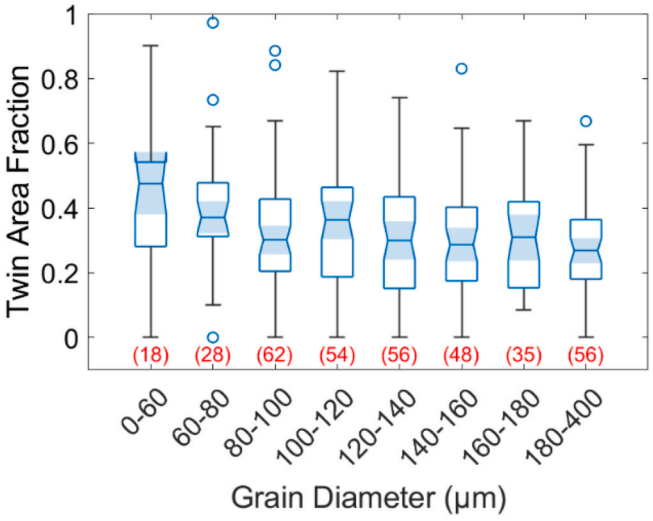

Fig. 7. Distribution of grain twin area fraction at a globally applied strain of $\varepsilon^G = -0.039$, with twinned grains binned by diameter. The twinned area fraction of a grain decreased slightly with increasing grain size, but the difference between most groups was not significant. The number of observations in each group is indicated by the red text in the parentheses above the bottom axis.

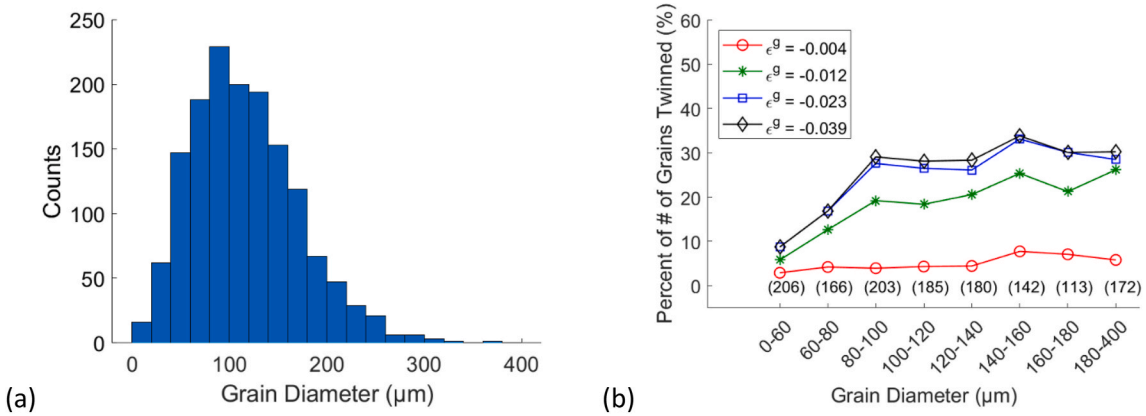

Fig. 6. (a) The grain size distribution of the WE43 sample, b) Ratio of twinned to total number of grains, binned by the grain diameter, at four different globally applied strains. There are nominally 100–200 grains in each grain diameter bin, indicated by the text in the parentheses above the bottom axis. The first and last grain diameter bins were adjusted to a larger size as there were very few grains with very small/large grain diameters.

summarizes the distribution of the twin area fraction inside each grain at $\varepsilon^G = -0.039$, with twinned grains binned by diameter. Most bins contain 30-60 grains, as indicated by the text in the parentheses above the bottom axis. The twinned area fraction of a grain decreased slightly with increasing grain size, but the difference between most groups was not significant. This observation differs from Reference [10], where twin area fraction was observed to increase with increasing grain size.

Grain size did not significantly affect the distribution of the grain-averaged effective strain in either non-twinned or twinned grains. Fig. 8(a) and (b) summarize the distribution of the grain-averaged effective strain for non-twinned and twinned grains, respectively, at $\varepsilon^G = -0.039$. Grains are binned by their diameter. Overall, no significant difference was observed in the distribution of the grain-averaged effective strain for grains within different diameter bins.

3.4. Effect of grain boundaries and neighboring grains on twinning

The effect of grain boundaries and neighboring grains on the selection and growth of twin variants was investigated. We use the following nomenclature:

- *Active twin system*: Twin systems visible on the DIC strain map.
- *Possible twin systems*: All six extension twin systems in each grain.
- *Available deformation modes in the neighboring grain*: To examine the effect of the deformation of the neighboring grain on twin variant selection in the grain of interest, we considered the *available deformation modes in the neighboring grain*, which are only a part of all deformation modes in the neighboring grain. If the active twin systems in the neighboring grain intersected the grain boundary *at or prior to* the strain level under consideration, those twin systems were considered. Otherwise, only basal slip systems in the neighboring grain were considered. In addition, the slip/twin system considered must have a nominal SF > 0.2, or a nominal SF normalized by the maximum nominal SF of these slip (twin) systems >0.8. These criteria were applied to reduce the total number of deformation systems under consideration in the neighboring grain to the ones most likely to be active and to interact with the twin system in the grain of interest.
- *Nucleating grain boundary*: A grain boundary where a twin nucleated.
- *Terminating grain boundary*: A grain boundary where a growing twin terminated.
- *Intersecting grain boundary*: A grain boundary that a twin intersected, including both nucleating and terminating grain boundaries. Twin nucleation and growth were not continuously experimentally observed, and it was common that at the strain level a twin was first identified, it already spanned the grain and intersected two boundaries on two opposite sides of the grain, so the nucleating and terminating boundary could not be differentiated. Each intersecting grain boundary, and the strain level at which the twin system first intersected the grain boundary, were recorded.
- *Predominant twin nucleating grain boundary*: The experimentally determined grain boundary at which a twin system first nucleated in a grain.
- *Grain boundary zone*: The local area in a grain adjacent to the grain boundary.

Fig. 9 illustrates the different types of grain boundaries, by schematically considering the evolution of twinning at two strain levels in a microstructure containing seven grains labeled A-G. Grain boundaries are labeled by the grain pairs that form them. For example, for twinning observed in grain D, grain boundary AD was its nucleating grain boundary (at Strain Level 1), and grain boundary DE was its terminating grain boundary (at Strain Level 2). Both AD and DE were its intersecting grain boundaries, and AD was the predominant twin nucleating grain boundary. For the twinning observed in grain C (at Strain Level 2), both AC and BC were intersecting grain boundaries. As we cannot differentiate between the nucleating and terminating grain boundaries, both AC and BC were considered predominant twin nucleating grain boundaries.

A unique aspect of this work is the ability to track full-field strains during mechanical loading in order to correlate strain evolution and incipient twinning; for example, one can investigate the state of a region that is about to twin, and the state of its surrounding neighborhood. Hypothetically, twinning in a grain depends on the presence of existing slip and twinning in its neighboring grains. Based on the assumption that twinning nucleates at grain boundaries, we focused our investigation on the grain boundary area, where one grain was considered as the *grain of interest*, and the other grain was considered as the *neighboring grain*. The grain boundary zone in the grain of interest was classified into a category, based on the deformation modes in the grain boundary zones on each side of the grain boundary, from the following: (1) no twinning observed, therefore inferred as slip-dominated deformation, (2) newly twinned at this strain level, and (3) pre-existing twin from a previous strain level. Considering both sides of the grain boundary, this results in nine possible combinations. In each grain under examination, the grain boundary zone was classified into one of nine categories, summarized in Table 1 and illustrated in Fig. 9. Note that as a grain boundary is shared between two grains, each grain boundary was assessed twice. Each time, the grain boundary zone in one of the two grains sharing the grain boundary was assessed. For example, at Strain Level 1, twinning was not observed at grain boundary AB. Twinning nucleated at grain boundary AB into grain B at Strain Level 2, and this is categorized as slip-induced twin nucleation, i.e., twinning in grain B was induced by slip in grain A. Therefore, the grain A side of grain boundary AB is designated as "category 2", as grain A was not twinned and the neighboring grain B

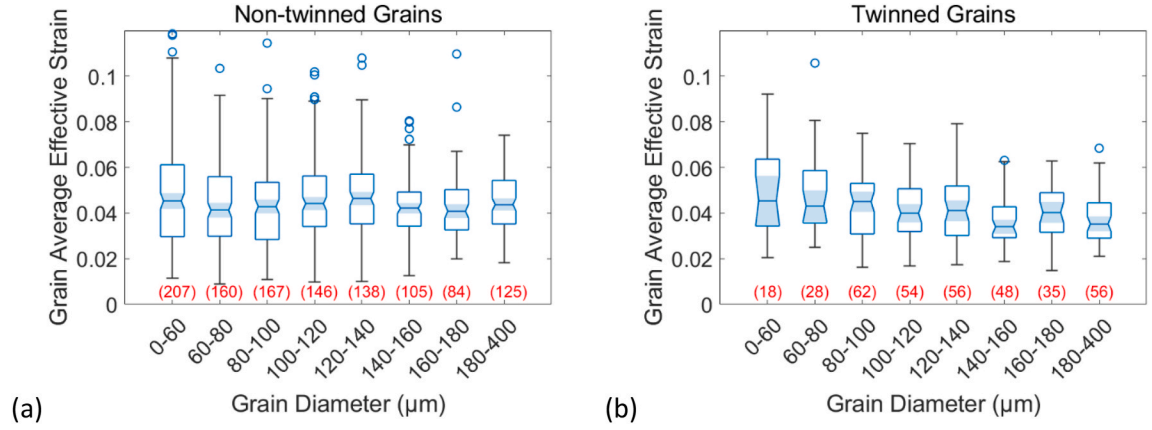

Fig. 8. The distribution of the grain-averaged effective strain of grains that were (a) not twinned, and (b) twinned, at a globally applied strain of $\varepsilon^G = -0.039$, with grains binned by their diameter. The number of observations in each group is indicated by the red text in the parentheses above the bottom axis.

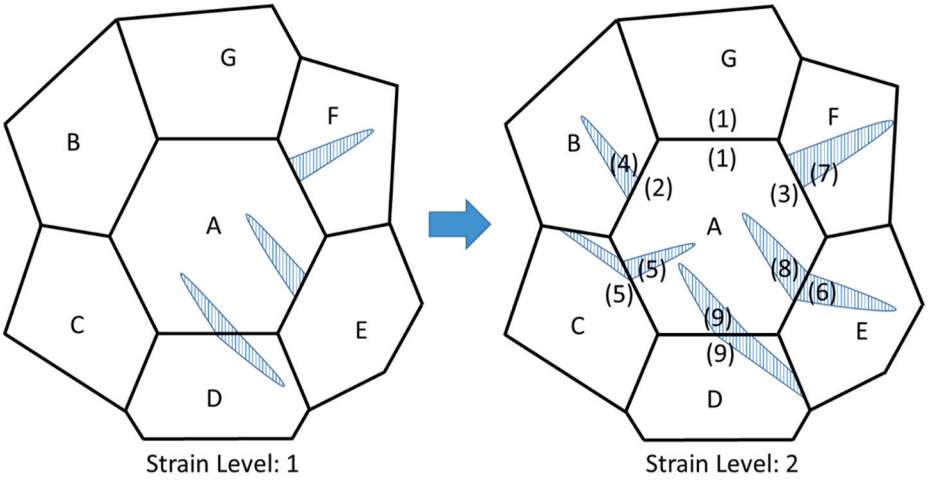

Fig. 9. A schematic microstructure illustrating the types of grain boundaries and grain boundary zones. Twinned areas are marked with stripes, and the twin evolution at two strain levels in grains labeled by letters A – G is shown. The categories of grain boundary zones are marked by numbers in parentheses near grain boundaries that refer to those tabulated in Table 1, and discussed in the text.

Table 1
Categories of the grain boundary zone *in the grain of interest* based on the deformation activity on each side of the grain boundary at a given strain level.

		Activity in the neighboring grain		
		Not twinned	Newly twinned	Pre-existing twin
Activity in the grain of interest	**Not twinned**	(1) No twinning activity	(2) Slip-induced twin nucleation	(3) Slip-induced twin growth
	Newly twinned	(4) Slip-induced twin nucleation	(5) Co-twin nucleation	(6) Twin-induced twin nucleation
	Pre-existing twin	(7) Slip-induced twin growth	(8) Twin-induced twin nucleation	(9) Co-growth of twinning

was newly twinned. The grain B side of grain boundary AB is designated as "category 4", as grain B was newly twinned and the neighboring grain A was not twinned.

A summary of the number of incidents of the nine categories of grain boundary zones at each of the global strains is provided in Table 2. Of the 1515 grains examined using SEM-DIC, a total of 8612 grain boundary zones were characterized and classified. At the maximum global compression $\varepsilon^G = -0.039$, twins were observed in 357 out of 1515 grains; and 1310 out of 8612 grain boundary zones exhibited twinning. The incidents represented in these tables are instantaneous values determined at each applied strain level, and thus the grain boundary zone categories can fluctuate with applied strain and either increase or decrease. Most grain boundary zones did not contain twins at any strain level (Table 2). Even at the highest strain, twins were only observed in 2026 out of the 8612 grain boundary zones. Category 3 and 7 are the predominant categories which indicates that twin growth is generally associated with slip in adjacent grains. Categories 2, 4 and 5, which represent slip-induced twin nucleation are prevalent at low strains and decrease as strain increases. Presumably these reflect the transition to twin growth represented by Categories 3 and 7. Categories 5, 6 and 8 occur in relatively few grain boundary zones. These categories represent twin nucleation due to twinning in an adjacent grain which appears to be infrequent.

Table 2
The number of incidents of the 9 categories of grain boundary zones at a global strain of $\varepsilon^G = -0.039$.

Global Strain ε^G	Grain Boundary Zone Category								
	1	2	3	4	5	6	7	8	9
−0.004	8354	122	0	122	14	0	0	0	0
−0.012	7338	469	107	469	78	15	107	15	14
−0.023	6614	350	532	350	24	44	532	44	122
−0.039	6328	140	850	140	6	32	850	32	234

3.4.1. *Strain distribution characteristics*

In this section, we analyze the effective strain distribution in the grain boundary zone of different categories. The classification of the grain boundary zone depends on the active deformation mechanisms at strain level *N*. However, the strain data at strain level *N*-1 are summarized for analysis, as this enables examination of the relationship between twinning and the strain distribution prior to twinning. For each grain boundary zone *k* of category *j*, let *d* represent the distance between a data point and the grain boundary, with all distances rounded to integer values. The mean effective strain of all the data points with the same distance to the grain boundary, denoted by $f_{kj}(d)$, was calculated as:

$$f_{kj}(d) = \frac{1}{N_d}\sum_{i=1}^{N_d}\varepsilon_{eff}^{d}(i) \quad \text{Eq. (2)}$$

where N_d is the number of data points with distance d to the grain boundary, and $\varepsilon_{eff}^{d}(i)$ is the effective strain of data point i with distance d to the grain boundary. For each grain boundary zone category j, the $f_{kj}(d)$ values of all grain boundary zones of that category were averaged again, to represent the mean effective strain distribution for this category of grain boundary zone:

$$F_j(d) = \frac{1}{M}\sum_{k=1}^{M} f_{kj}(d) \quad \text{Eq. (3)}$$

where M is the number of grain boundary zones in the category considered. The mean effective strain distribution in different categories of grain boundary zones was summarized at different globally applied strains (ε^G) in Fig. 10. Caution should be taken when comparing the strain distribution in a twin-containing grain boundary zone to that in a slip-dominated grain boundary zone, as the intensity of slip deformation can be represented by its associated strain field, whereas twinning exhibits a fixed twin shear and associated strain. Other measures, such as the twinned area, may better represent the intensity of twinning deformation.

Only four categories of grain boundary zones existed at $\varepsilon^G = -0.004$,

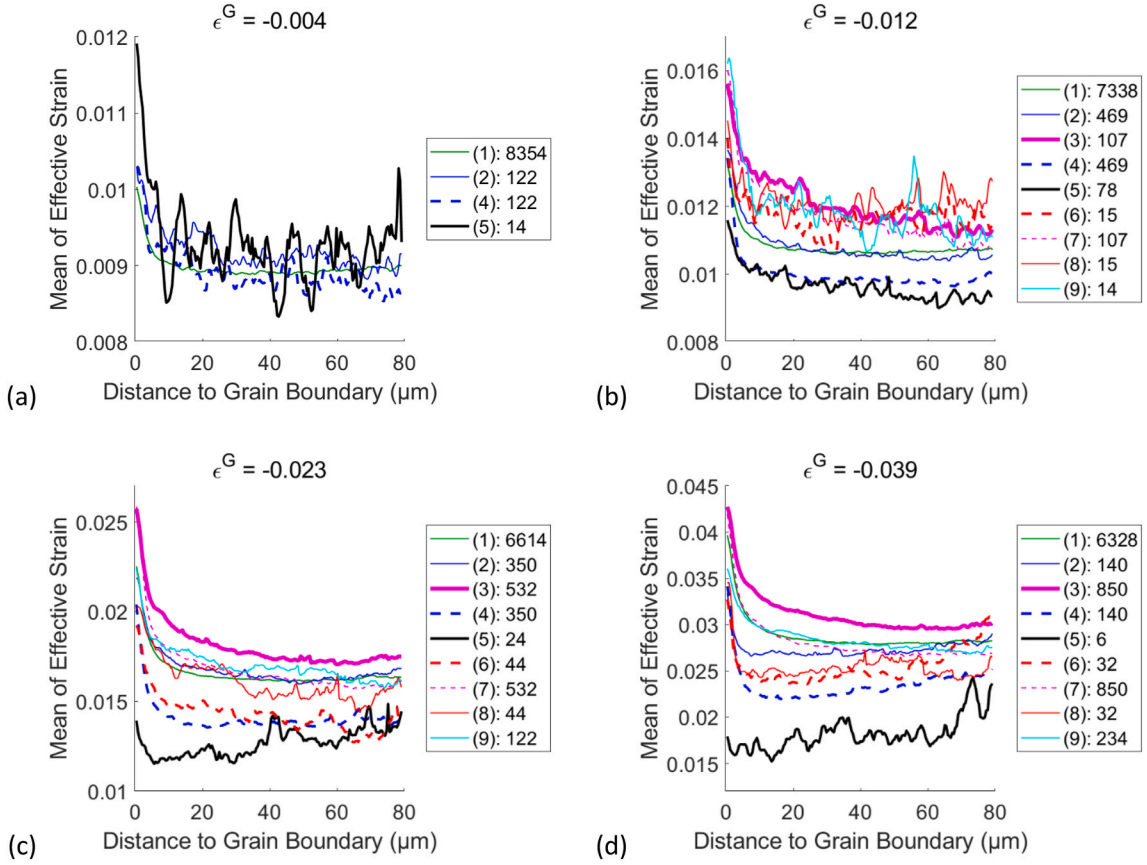

Fig. 10. The experimentally measured strain distribution in the grain of interest in the nine categories of grain boundary zones at four different globally applied compressive strains. The legend indicates the grain boundary zone category from Table 1 (in parentheses), and the number of incidents for each category. A total of 8612 grain boundary zones were characterized of which only 1310 ultimately exhibited the presence of twinning at $\varepsilon^G = -0.039$.

which was the lowest strain level where twins were identified, as shown in Fig. 10(a). There was no noticeable difference observed between the strain distributions in the four categories, possibly because there was a low signal to noise ratio at this small ε^G.

Twinning appears to activate in order to accommodate existing deformation in a neighboring grain. This is seen in Fig. 10(b)–(d), where regions that were more likely to initiate twinning in their neighboring grain exhibited higher strains. Prior to twinning nucleation, areas generally exhibited limited deformation. This trend became more distinct as the globally applied strain increased.

The 9 categories of grain boundary zones (Table 1) can be roughly divided into 3 groups:

(1) In the case of slip-induced twin growth, the side of the grain boundary with active slip (category 3) exhibited the largest strain among these 9 categories. One possible explanation is that this type of grain boundary zone is one in which slip activated the easiest. The continuous buildup of dislocations caused early twin nucleation in the neighboring grain and provides a driving force for twin growth.
(2) Areas that were about to twin exhibited very low strains in the load step immediately prior to twinning nucleation. These areas included 3 categories: the co-twin nucleation area (category 5), the new twin side of the slip induced twin nucleation (category 4), and the new twin side of the twin induced twin nucleation (category 6). These areas were likely less favorable for slip activity.
(3) The remaining 5 categories exhibited medium strain, which included 2 slip dominated areas (those not involved in twinning activity - category 1, and the slip side of the case of slip-induced twin nucleation - category 2), and 3 twin-containing areas (the old twin side of twin-induced twin nucleation - category 8, the twin side of slip-induced twin growth - category 7, and areas with co-growth of twinning activity - category 9). This means that after a twin has been activated, the strain in these areas (the 3 twin-containing areas) tend to increase to a similar level to the strain in areas (the 2 slip dominated areas) that were about to activate new twinning or slip in neighboring grain.

3.4.2. *Effect of m' factor*

To study the correlation between geometric compatibility and twinning, the m' factor [19,20] was calculated between each of the six extension twinning systems (including both active and non-active) in the grain of interest, at each of the grain boundaries with each *available* slip/twinning system in the neighboring grain, and at each globally applied strain level. The m' factor, defined as $m' = \cos(\kappa)\cos(\psi)$, where κ is the angle between two slip/twin directions, and ψ is the angle between two slip/twin plane normal directions, is used to describe the geometric compatibility between two slip/twin systems across a grain boundary. An m' factor of 1 means the two slip/twin systems are completely compatible, where the slip/twin planes are parallel and the slip/twin direction are the same. An m' factor of 0 indicates the two slip/twin systems are completely incompatible, and either the slip/twin planes or the slip/twin directions are orthogonal. An m' factor of -1 means the slip/twin planes are parallel, but the slip/twin directions are opposite. For each considered twin system, whether active or not, there is an m' value with each of the potential slip or twin systems in the neighboring grain.

To simplify the analysis, the largest m' value between the considered twin system and all available deformation modes (either slip or

twinning) in the neighboring grain, defined as M′, was selected to represent the geometric compatibility. The definition of 'available deformation modes in the neighboring grain' can be found at the beginning of section 3.3. The probability distribution of the M′ factor was investigated for its effect on twin nucleation. Rather than examining the M′ distribution for active twin systems, it is more important to examine how it compares with that of randomly selected twin systems (regardless of active or not) in the sample. This is because, for example, if it is frequent to observe large M′ values in active twin systems, it does not necessarily mean a large M′ is correlated with the ease of twin nucleation if it is also frequent to observe large M′ values in randomly selected twin systems. The comparison between the distributions was made by taking the ratio of the probability mass function of these two distributions. The probability mass function (p) was calculated using the following equation:

$$p(X \in B_i) = N_i / N \quad \text{Eq. (4)}$$

where N_i is the number M′ factors with a value in the bin B_i and N is the total number of M′ factors.

A high M′ value was found to be correlated with the nucleation of a twin variant. Fig. 11 summarizes the probability mass function of experimentally-determined M′ values for all active twin systems at their *predominant twin nucleating* grain boundaries with available slip or twinning systems in the neighboring grain, the M′ for all *possible* twin systems with available slip or twinning systems in the neighboring grain (which represents the M′ distribution for randomly selected twin systems in the specimen), and the ratio between these two functions at $\varepsilon^G = -0.039$. The population size of the M′ values are indicated in the legend. The M′ distribution suggests that it is not necessary for an active twin system to exhibit a high M'. However, the ratio between the two distributions became larger than 1 when M′ reached approximately 0.8, indicating that it is more frequent to observe an M′ larger than 0.8 in an active twin system than in randomly selected twin systems, and could be up to 6 times higher than a random density as the M′ value approached 1. This does indicate a correlation between a high M' value and twin nucleation. When M′ was negative, the ratio exhibited fluctuations due to the small number of samples in this range.

The effect of M′ rank was also analyzed. At each grain boundary, the M′ values of the six twin systems were ranked in descending order from 1 (highest) to 6 (lowest). The effect of M′ rank on twin variant selection is not significant, although there is a slight tendency that active twin variants are more likely to have the highest M′ rank.

Fig. 12 summarizes the probability mass function of the M′ rank for all active twin systems at their predominant twin nucleating grain boundaries with the available slip or twinning systems in the neighboring grain, the M′ rank for *all* possible twin systems with the available slip or twinning systems in the neighboring grain, and the ratio between these two distributions. The active twin variants exhibit a larger probability (~0.36) to have the highest M′ rank. However, there were a significant number of active twin systems with the other M′ ranks, including at the lowest M′ values (rank 5 and 6). For the M′ rank for *all* possible twin systems with the available slip or twinning systems in the neighboring grain, there are slightly more twin systems with M′ ranked 1. This is because not all of the potential twin systems have an available slip or twinning system in the neighboring grain (see the definition of 'available deformation modes' at the beginning of section 3.3). According to the ratio between these two functions, an active twin system with an M′ rank of 1 was observed approximately twice as frequently as the randomly selected twin systems. In a study by Guan et al. [15], more than 80% of active twin variants exhibited the 1st or 2nd highest m' rank; the current study did not find as distinct a differentiation in the M′ rank of active twins.

3.4.3. *Effect of residual burgers vector*

Another metric that represents the geometric compatibility of two slip/twinning systems in neighboring grains is the residual Burgers vector [44]. At each grain boundary and global strain, ε^G, the residual Burgers vector was calculated between each of the six extension twin systems in the grain of interest and each *available* slip/twinning system in the neighboring grain. The smallest residual Burgers vector between the considered twin system and all available slip/twin systems in the neighboring grain was selected (defined here as *RBV*) to represent the geometric compatibility of that twin system with the available deformation modes in the neighboring grain. In addition, at each grain boundary, the RBV values of the six twin systems were compared and ranked in ascending order from 1 (the smallest) to 6 (the largest), termed the *RBV rank*.

The probability mass function of the RBV for active twin systems at their predominant twin nucleating grain boundaries with the available slip or twinning systems in the neighboring grain, for all possible twin systems with the available slip or twinning systems in the neighboring grain, and the ratio between these two probability mass functions are shown in Fig. 13(a). Fig. 13(b) performs the same analysis to RBV rank.

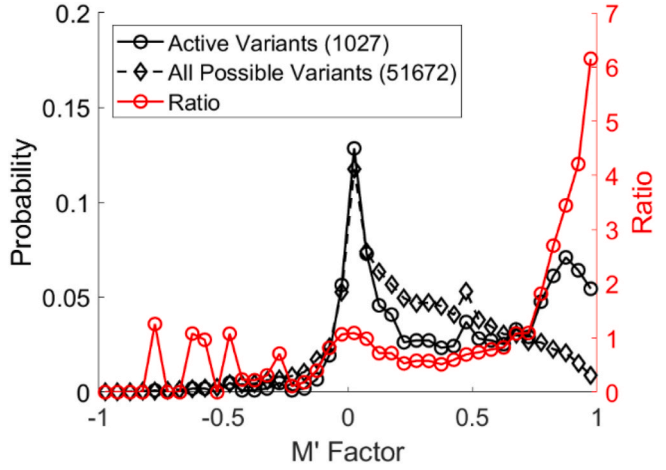

Fig. 11. The probability mass function of M′ for active twin variants at their predominant twin nucleating grain boundaries with available slip or twin systems in the neighboring grain, for all possible twin variants with available slip or twin systems in the neighboring grain, and the ratio of these two functions at $\varepsilon^G = -0.039$. The population size of the M′ factors is indicated by the number in the parentheses in the legend.

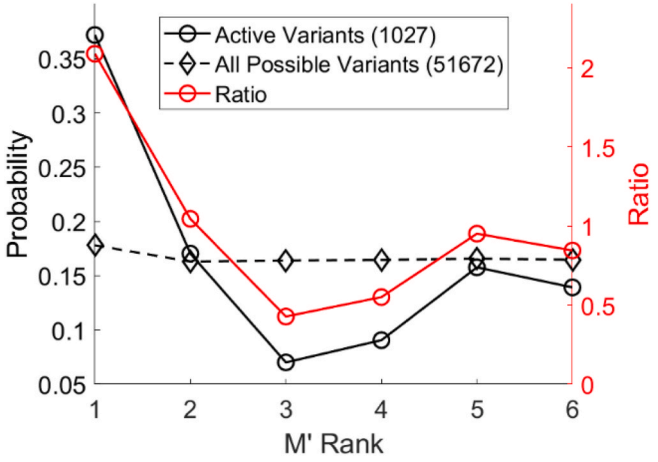

Fig. 12. The probability mass function of the M′ rank for active twin systems at their predominant twin nucleating grain boundaries with the available slip or twinning systems in the neighboring grain, for all possible twin systems with available slip or twinning systems in neighboring grain, and the ratio between these two functions, at a globally applied strain of $\varepsilon^G = -0.039$. The population size of the distributions is indicated by the text in the parentheses in the legend.

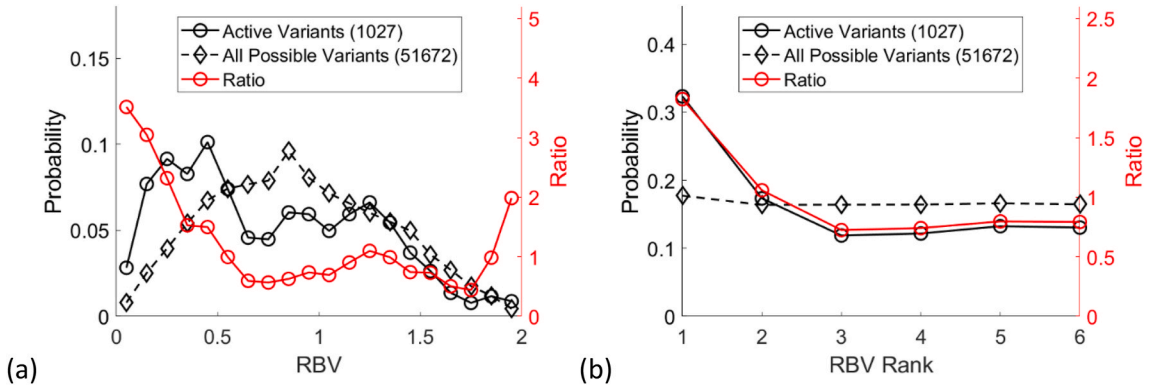

Fig. 13. The probability mass function of the (a) RBV and (b) RBV rank for the active twin systems at their predominant twin nucleating grain boundaries with available slip or twinning systems in the neighboring grain, for all possible twin systems with available slip or twinning systems in the neighboring grain, and the ratio between these two functions, at a globally applied strain of $\varepsilon^{G} = -0.039$. The population size of the distributions is indicated by the number in the parentheses in the legend.

In comparison to a randomly selected twin system, a larger percentage of the active twin systems exhibited an RBV smaller than 0.5, and exhibited the 1st rank (smallest) RBV. However, the maximum ratio of the probability mass functions was relatively small, and this suggests that the effect of RBV or RBV rank on twin variant selection is smaller than that of M'.

3.4.4. *Effect of strain accommodation*

The effect of strain accommodation on twin variant selection was examined using a similar approach to Ref. [17]. Briefly, for a given twin system, the displacement gradient tensor (e_{ij}) was transformed into the coordinate system of a given deformation mode M (including basal slip, prismatic slip, pyramidal <*a*> slip, 2nd order pyramidal <*c*+*a*> slip, and extension twinning) of the neighboring grain. A parameter, e^{M}_{xz}, which is the maximum of the *xz*-component of the transformed displacement gradient tensors, was used to represent the strain accommodation that needs to be provided by deformation mode M in the neighboring grain. Based on e^{M}_{xz}, two additional parameters, γ^{M} and ϵ^{M}, were also introduced by Shi et al. [17] to evaluate the extent of high demand and low demand of the accommodation deformation modes. Details for the calculation and interpretation of the parameters are provided in Appendix B.

In the current work, the effect of the strain accommodation parameters (such as e^{M}_{xz} and γ^{M}) on twin variant selection had minimal significance; only e^{basal}_{xz} exhibited a slight correlation with active twin variants. Fig. 14 summarizes the probability mass function of e^{basal}_{xz} for the active twin variants and all possible twin variants, and the ratio between these two probability mass functions. The active twin variants were slightly more likely to exhibit an $e^{basal}_{xz} > 0.1$. However, the maximum ratio was about 1.5 times higher than a random density, which suggests that the effect of e^{basal}_{xz} on twin variant selection is smaller than that of m'. Apart from the slight correlation of e^{basal}_{xz} shown in Fig. 14, none of the strain accommodation parameters exhibited significant correlation with twin variant selection. Therefore, the strain accommodation models found in the literature [12,13,17] do not fully explain the experimental observations of this work.

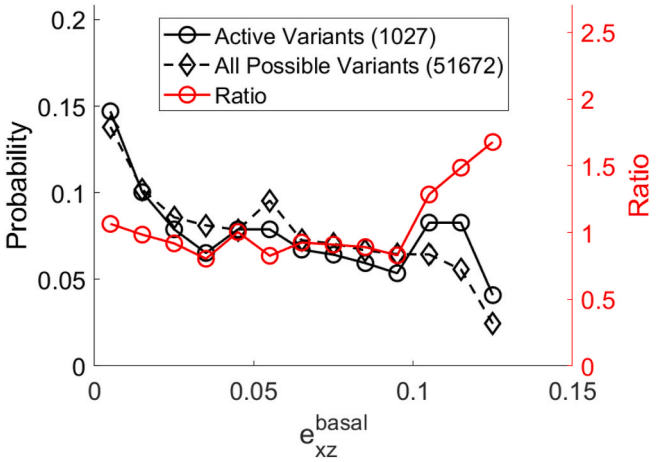

Fig. 14. The effect of the strain accommodation parameter e^{basal}_{xz} (as defined in section 3.3.5) on twin variant selection had minimal significance. The plot shows the probability mass function of e^{basal}_{xz} for active twin systems at their predominant twin nucleating grain boundaries and for all possible twin systems in the sample, and the ratio between the two functions. All plots were for a globally applied strain of $\varepsilon^{G} = -0.039$. The population size of the distributions is indicated by the text in the parentheses in the legend.

3.5. *PRISMS-plasticity CPFE simulation of SEM-DIC experiment*

The multiscale rate-independent crystal plasticity model developed by Yaghoobi et al. [24] was incorporated in the current work to simulate the response of WE43-T6 sample. The details of the selected model have been published elsewhere [36–39] and an overview is provided in Appendix A. Four slip modes including basal $\langle a \rangle$ ($\{0001\}\langle 11\bar{2}0\rangle$), prismatic $\langle a \rangle$ ($\{10\bar{1}0\}\langle 1\bar{2}10\rangle$), pyramidal $\langle a \rangle$ ($\{10\bar{1}1\}\langle 1\bar{2}10\rangle$), and pyramidal $\langle c+a \rangle$ ($\{11\bar{2}2\}\langle \bar{1}123\rangle$), along with one extension twin mode ($\{10\bar{1}2\}\langle \bar{1}011\rangle$) were considered in modeling the WE43-T6 alloy in this work. Similar to other work by the authors, Githens et al. [36] and Yaghoobi et al. [38], the precise boundary conditions for the simulated sample were extracted from the experimentally-obtained displacement map using an automated pipeline procedure linked with the PRISMS-Plasticity CPFE code. The displacement map was measured on the traction-free sample surface, and therefore a plane-stress assumption was used [36,38]. Accordingly, a 3D plate with the thickness to length ratio of 0.1 was used for all simulations. Since no variation of the variables *u* and *v* was expected in the *z*-direction, a single layer of elements was assumed in the *z*-direction along with a 500 × 400 mesh. Githens et al. [36] compared the results of the generated columnar sample versus 3D sample, and showed that generalized plane-stress on a columnar grain structure (as the surface is traction free) exhibited a good match to the SEM-DIC results.

The rate-independent crystal plasticity model was calibrated for the WE43-T6 sample by Yaghoobi et al. [38] using its uniaxial compression and tension responses. The simulation microstructure including texture and grain morphology was generated using the experimental data presented in Fig. 1. Yaghoobi et al. [38] also incorporated twinning data to calibrate the twinning parameters of the crystal plasticity model. The

elastic constants of pure Mg at room temperature [24,30,38] were incorporated into the CPFE model and are presented in Table 3. Table 4 presents the crystal plasticity parameters for slip and twinning modes were determined previously [39] but are provided here for completeness. The twin can grow due to the parent reduction, i.e., twin nucleation (Operation A), and/or child propagation, i.e., twin growth (Operation *B*). As described by Qiao et al. [45] and Yaghoobi et al. [24,38], the CRSS for twin nucleation is higher than that of twin growth, which can mimic the stress relaxation due to twinning. The latent hardening ratio of $q = 1.4$ was used for the slip deformation according to the Ganesan et al. [37] and Yaghoobi et al. [38]. In the case of latent hardening ratio for twinning, following Qiao et al. [45] and Yaghoobi et al. [24], the latent hardening ratio q was taken to be 1 for operations A and B.

The effect of the maximum basal Schmid factor and twin variants Schmid factor on the twinned grain ratio were investigated for the region of the sample that was simulated by PRISMS-Plasticity, as shown in Fig. 15. The PRISMS-Plasticity simulation shows minimal activity of twin variants with SF < 0.2 which is similar to the SEM-DIC results as shown in Fig. 15(a). As the twin variant SF increases, the proportion of twinned variants increases in both the PRISMS-Plasticity simulation and SEM-DIC results. Furthermore, the twinning propensity increased as the basal nominal SF decreased in both the CPFE and SEM-DIC results as shown in Fig. 15(b). This relationship was observed more strictly in the PRISMS-Plasticity simulation than in the experimental SEM-DIC results. This can be attributed to the application of a deterministic rule to model twinning in PRISMS-Plasticity. Fig. 15 shows that PRISMS-Plasticity overpredicted the experimental ratio of twinned grains.

The twin variant area fraction in each grain, which can be obtained as the active twinned area of that variant divided by the total area of the parent grain, is plotted versus the nominal twin variant SF in Fig. 16 for both PRISMS-Plasticity and SEM-DIC using box plots. The active twin variants were binned by their nominal SF, at a globally applied strain $\varepsilon^{G} = -0.039$. In both PRISMS-Plasticity simulation and SEM-DIC, the largest twin area fractions occurred for twin variants with the highest nominal SF. The standard deviation as represented by the box plots were similar for both experimental and simulation, which suggests that PRISMS-Plasticity reasonably captures the appropriate factors affecting twin variant selection.

4. Discussion

4.1. Effect of grain features and geometric compatibility

The SF is a good indicator for the likelihood of twin activation. It describes the ratio of the externally applied stress resolved to activate the slip/twin system based on a pure geometric consideration. The WE43 alloy in the current study has a weak texture. As shown in Fig. 3 (a), there were many slip/twin systems in each SF bin, making the sample proper for statistical analysis. Fig. 3(a) shows that twin variants with high SF are more likely to nucleate, and Fig. 4 shows that once nucleated, twins with high SF are easier to grow into a larger area fraction within their parent grain. However, it is clear from Fig. 3 that the SF alone does not have a deterministic effect on twinning. The local stress differs from the global stress because grains of different orientations react differently to applied stresses, and neighbor grains interact with each other. In addition, twin nucleation is often considered to be a process with stochastic nature [3]. Slip and twinning are competing mechanisms. As shown in Fig. 5(a), grains with high maximum basal SF show relatively high strain, most likely due to the high activity of basal slip, and these grains are less likely to twin, as suggested by Fig. 3(b).

Grain size appears to have little effect on twinning in the current study. However, it should be noted that the grain size was obtained from 2D surface measurements, which may not represent the grain size in 3D. In addition, the range of grain size is limited, where about 95% of the grains exhibited diameter within the range of 30 μm–240 μm. Therefore, the conclusion should be interpreted with caution.

Table 3
The elastic constants (MPa) of pure Mg at room temperature [24,30,38].

C11	C12	C13	C33	C44
59,400	25,610	21,440	61,600	16,400

Table 4
The calibrated values of initial slip resistance and corresponding hardening parameters for slip and twinning modes of WE43-T6 Mg alloy [36].

Mode	s_0^α (MPa)	h_0^α (MPa)	s_s^α (MPa)	a^α
Basal	47.6	250	144.4	2.5
Prismatic	92.2	350	289.0	2.5
Pyramidal<a>	104.5	350	347.5	2.5
Pyramidal<c+a>	117.3	350	304.9	2.5
Twinning (operation A)	93	1000	350	2.5
Twinning (operations B)	85	1000	320	2.5

4.2. Effect of geometric compatibility

Considering the effect of neighbor grains, the m' factor is a good indicator for deformation system alignment, as it considers both the alignment of the slip/twin plans and the slip/twin directions. However, it is based on pure geometric consideration. It does not describe the strain fields in the grain of interest, and it does not describe the amount of deformation occurred in the neighboring grain which might stimulate twin nucleation in the grain of interest. In the current study, the maximum m' factor, M′, was shown to be a more important factor compared to other metrics including the M′ rank, the RBV, and the RBV rank. However, there are many more grain boundaries than grains, and there are many pairs of slip/twinning modes to consider at each grain boundary. As shown in Fig. 11, the absolute number of active twin systems (1027) is much smaller than the total number of twin variants (51627) that could possibly be activated. Therefore, it is not reasonable to expect the m' alone to be a reliable metric to predict twin activation.

The current study concluded that the M′ factor correlates with twin variant selection. However, the effect appears to be much less dominant compared to that in Guan et al. [15] and Liu et al. [14], where more than 80% of the active twin variants were variants with high m' value and of 1st or 2nd rank. In the current study, the effect of m' factor was demonstrated from a different perspective, that is, by comparing the probabilities of high M′ values between active and possible twin variants (Fig. 11). The current study observed a wide range of M' values for active twin variants, which is also observed in Reference [17], although it did not reach a similar conclusion as the current study.

4.3. Strain accommodation models

The effect of strain accommodation on twin nucleation has been proposed in a series of work [11–13,17], with the idea that twin nucleation requires strain accommodation in the neighboring matrix, and the ease of such strain accommodation can affect twin variant selection. In Martin et al. [11], the activation of the low SF secondary extension twins in AM30 was attributed to the low accommodation strain required in the matrix of the parent grain, represented by the large angle between the shear direction of the secondary twin and the habit plan normal of the primary twin. Jonas et al. [12] extended this analysis to focus on low SF primary contraction twins in an AM30 alloy. The twinning shear displacement gradient tensor (e_{ij}) was rotated into the crystallographic reference frame of the neighboring grains, and the tensor components were subsequently correlated with different slip and twinning modes. Later, Mu et al. [13] extended this analysis to three generations of twins (i.e. primary, secondary, and tertiary) in an AZ31 alloy. Both studies [12,13] found the importance of strain

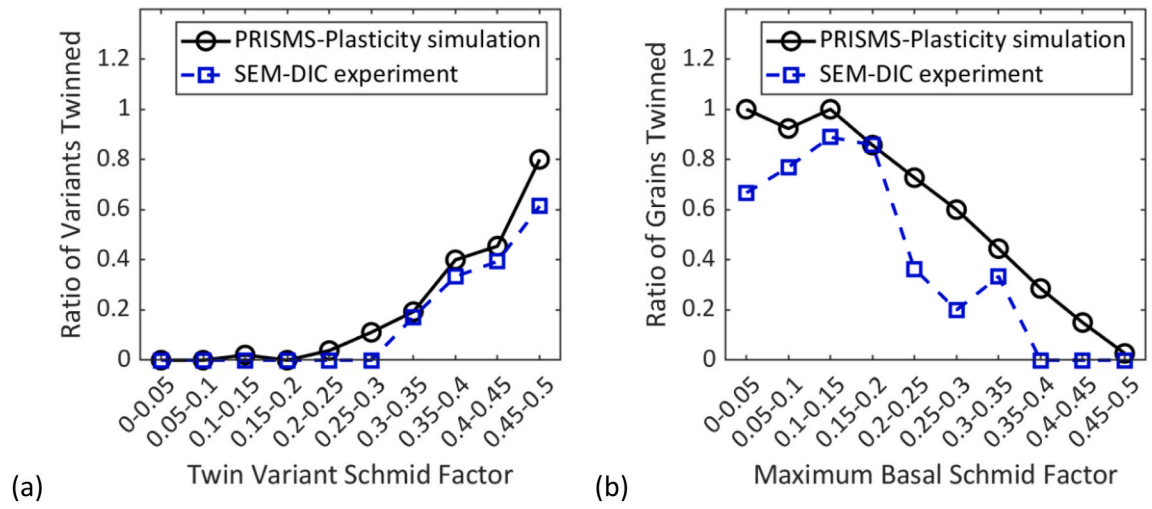

Fig. 15. The effect of nominal Schmid factor on twinning obtained by either SEM-DIC experiment or PRISMS-Plasticity simulation at a globally-applied compressive strain, ε^{G}, of −0.039. (a) The ratio of variants that are twinned, i.e., the number of twinned variants divided by the total number of variants, versus their nominal Schmid factor. (b) The ratio of grains that are twinned, i.e., the number of twinned grains divided by the total number of grains, versus their maximum nominal basal Schmid factor.

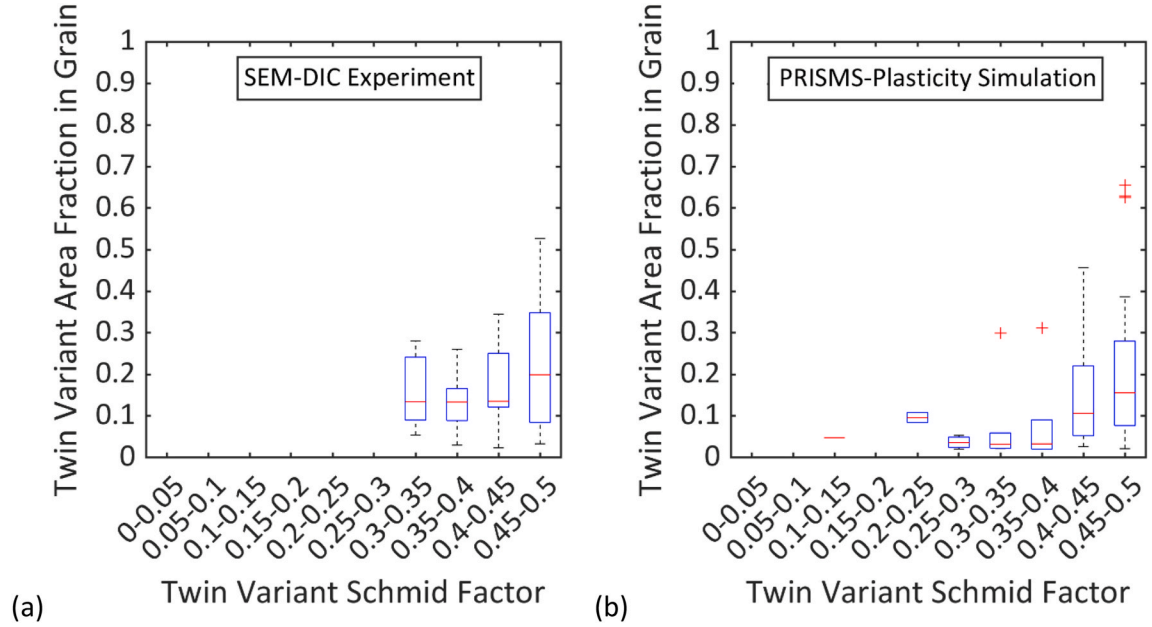

Fig. 16. Box plot summarizing the distribution of the active twin variant size represented as the area fraction of their parent grain, where the active twin variants were binned by their nominal SF, at a globally applied strain of −0.039: (a) SEM-DIC experiment and (b) PRISMS-Plasticity simulation. The largest twin area fractions occurred for twin variants with the highest nominal SF for both PRISMS-Plasticity simulation and SEM-DIC experimental results.

accommodation for twin variant selection, e.g., twins formed when they require least accommodations by prismatic slip in the neighboring grain. However, References [12,13] failed to consider crystal symmetry, so the analysis was in fact not based on an unambiguous value representing the strain accommodation. Shi et al. [17] studied low SF extension twins in Mg AZ31, and found that active twin variants with a low SF either: (1) required greater accommodation in the neighboring grain through basal slip, and less accommodation through pyramidal slip; or (2) required less accommodation through pyramidal slip and/or contraction twinning, and greater accommodation through prismatic slip and/or extension twinning. As described in Appendix B, the analysis took crystal symmetry into consideration, which is an improved approach compared to that in Refs. [12,13].

Although the strain accommodation models provided reasonable explanation for twinning activity in some studies [12,13,17], they were not able to explain the twin variant selection in the current study, shown in Section (3.4.4). The strain accommodation models suggest that certain types of deformation occur in the neighboring grain to accommodate twinning in the grain of interest, which means the accommodation strain in the neighboring grain should occur no earlier than twinning in the grain of interest. The current study, by performing unique analysis on the local strain evolution in different types of grain boundary zones, suggests the opposite. Instead of introducing accommodation deformation in the neighboring grain, twinning is more likely to accommodate deformation in the neighboring grain. In another word, the stimulation for twinning comes from the buildup of local stress/-strain concentration in the neighboring grain, whereas twinning reacts passively. It can be seen from Fig. 10 that, the grain boundary zones that

are about to twin exhibited lower strain compared to the grain boundary zones on the opposite side of the grain boundary. For example, the strain in grain boundary zone of category 4 is lower than that in category 2, and category 6 is lower than that of category 8. Due to the weak texture, many grains in the sample favors basal slip, and it can be seen from Fig. 10 that grain boundary zones with slip activity (categories 2 and 3) generally exhibit high strain, which agrees with their role of driving twin nucleation and growth in the neighboring grain.

5. Summary

The effect of microstructure and microstructural neighborhoods on the nucleation and growth of deformation twinning in WE43-T6 Mg under in situ compression was examined. Deformation twinning was identified from the full-field strain evolution, which was characterized by digital image correlation inside a scanning electron microscope. Over 1515 individual grains and 8612 grain boundary zones were characterized. Based on a statistically significant number of observations, the following was concluded:

(1) Consistent with prior literature, the macroscopic nominal Schmid Factor significantly affected twinning nucleation and growth. The nominal SF is an important variable affecting both twinning activation and twin variant size, as twinning statistics from CPFE compared well with experimental observation. Twin variants with a higher twin Schmid Factor were more likely to nucleate. Twinning nucleation in grains with a high maximum basal SF was unlikely. Twin variants with higher twin Schmid Factors accounted for a larger area fraction of their parent grains and exhibited a larger scatter in that area fraction. The effective strain distribution positively correlated with basal Schmid factor in grains that did not twin.
(2) SEM-DIC experiment showed that the grain size effect on twinning is not considerable. The number fraction and area fraction of twinned grains did not vary significantly with grain diameter. The effective strain was similar in grains of various sizes.
(3) The maximum m' factor, M′, exhibited a moderate correlation with twin variant selection. This correlation was slightly larger compared to the M′ rank, residual Burgers vector, and residual Burgers vector rank which had a low correlation with twin variant selection. The effect of m' factor was demonstrated by comparing the probabilities of high M′ values between active and possible twin variants, which is a new perspective comparing to existing literature.
(4) Unique analysis on the local strain evolution in different types of grain boundary zones showed that the twinned areas correlated with grain boundary zone that exhibited relatively high strain in neighboring grains. This indicates that a buildup of a local stress/strain concentration occurs prior to the initiation of twinning in the neighboring grain. Strain accommodation models found in the literature do not fully explain the experimental observations of this work.
(5) CPFE simulation successfully captured the twin statistics and showed that the largest twin area fractions occurred for twin variants with the highest nominal SF. Also, the CPFE simulation accurately captured the effect of nominal Schmid factor on twinning. However, this relationship was observed more strictly in the CPFE simulation than in the experimental SEM-DIC results, which can be attributed to the application of a deterministic rule to model twinning in the CPFE framework.

6. Data and code availability

- The experimental data and PRISMS-Plasticity results files supporting this publication are available in the Materials Commons at DOI: http://doi.org/10.13011/m3-wkc3-th61, and DOI: https://doi.org/10.13011/m3-thgc-jj93.
- Input files for the PRISMS-Plasticity simulations can be downloaded from Materials Commons using the following link: https://materialscommons.org/mcapp/#/data/dataset/8125b518-4955-4a5f-b887-24bc5544af38.
- MATLAB codes for analyzing the SEM-DIC data are available on Github: https://github.com/chenzhe3701/DIC_Analysis.
- PRISMS-Plasticity software can be freely downloaded from the following link: https://github.com/prisms-center/plasticity.

CRediT authorship contribution statement

Zhe Chen: Writing – original draft, Investigation, Visualization. **Mohammadreza Yaghoobi:** Writing – original draft, Software, Visualization. **Veera Sundararaghavan:** Writing – review & editing. **John Allison:** Writing – review & editing, Funding acquisition. **Samantha Daly:** Writing – review & editing, Supervision.

Declaration of competing interest

The authors declare that they have no known competing financial interests or personal relationships that could have appeared to influence the work reported in this paper.

Data availability

Links to data are provided in the manuscript.

Acknowledgements

This work was supported by the U.S. Department of Energy, Office of Basic Energy Sciences, Division of Materials Sciences and Engineering under Award #DE-SC0008637 as part of the Center for PRedictive Integrated Structural Materials Science (PRISMS). This work used the Extreme Science and Engineering Discovery Environment (XSEDE), which is supported by the National Science Foundation grant number ACI-1548562, through the allocation TG-MSS160003.

Appendix A. Simulation Methodology: Crystal Plasticity Model

The multiscale rate-independent crystal plasticity model developed by Yaghoobi et al. [24] was implemented in the open source PRISMS-Plasticity CPFE software [39]. In this model, the contributions of both parent grain and twinned regions, called children, are included. The superscripts *mt* and *tw*, *k* in this section correspond to the parent and child nucleated due to the activation of the k^{th} twin system of the parent. In this model, the parent grain and twinned children at a material point are subject to the same deformation gradient tensor **F**. The multiplicative decomposition is [46]:

$$\mathbf{F} = \mathbf{F}^{e\,mt}\mathbf{F}^{p\,mt} = \mathbf{F}^{e\,tw,k}\mathbf{F}^{p\,tw,k} \quad \text{Eq. (A1)}$$

where $\mathbf{F}^e$ and $\mathbf{F}^p$ are elastic and plastic deformation gradient tensors, respectively.

The additive decomposition of macroscopic velocity gradient tensor **L** was performed as follows:

$$\mathbf{L} = \mathbf{L}^{emt} + \mathbf{L}^{pmt} = \mathbf{L}^{etw,k} + \mathbf{L}^{ptw,k} \quad \text{Eq. (A2)}$$

where $\mathbf{L}^{e}$ and $\mathbf{L}^{p}$ are the elastic and plastic velocity gradient tensors, respectively, defined as:

$$\mathbf{L}^{pmt} = \sum_{\alpha=1}^{N_s^{mt}+N_t^{mt}} \dot{\gamma}^{\alpha}\mathbf{S}^{\alpha}\,\mathrm{sign}(\tau^{\alpha}) \quad \text{Eq. (A3a)}$$

$$\mathbf{L}^{ptw,k} = \sum_{\beta=1}^{N_s^{tw}+N_t^{tw}} \dot{\bar{\gamma}}_{\kappa}^{\beta}\mathbf{S}_k^{\beta}\,\mathrm{sign}\left(\tau_k^{\beta}\right) \quad \text{Eq. (A3b)}$$

where the twinning systems are modeled as pseudo-slip systems. τ^{α}, $\dot{\gamma}^{\alpha}$, and $\mathbf{S}^{\alpha}$ are the resolved shear stresses, shearing rate, and Schmid tensor, respectively, on slip systems α in parent grain. τ_k^{β}, $\dot{\bar{\gamma}}_{\kappa}^{\beta}$, and $\mathbf{S}_k^{\beta}$ are the resolved shear stresses, shearing rate, and Schmid tensor, respectively, on β^{th} system of the k^{th} child. N_s and N_t are the number of slip and twinning pseudo-slip systems. N_t^{mt} is equal to twice the material twin systems, in which the first set corresponds to twin growth and the second set corresponds to twin shrinkage. In the current model, $N_t^{tw} = 2$ including one for twin growth and one for shrinkage inside the child, which is the same as the twinning system of the parent which generates that child.

The resolved shear stress, slip resistance, and yield surface in both parent and child are defined as:

$$\tau^{\alpha} = \boldsymbol{\sigma}^{mt} : \mathbf{S}^{\alpha}; \quad \tau_k^{\beta} = \boldsymbol{\sigma}_k^{tw} : \mathbf{S}_k^{\beta} \quad \text{Eq. (A4a)}$$

$$g^{\alpha} = |\tau^{\alpha}| - s^{\alpha}; \quad g_k^{\beta} = \left|\tau_k^{\beta}\right| - s_k^{\beta} \quad \text{Eq. (A4b)}$$

$$\dot{s}^{\alpha} = \sum_{\vartheta} h^{\alpha\vartheta}\dot{\gamma}^{\vartheta}; \quad \dot{s}_k^{\beta} = \sum_{\varphi} h_k^{\beta\varphi}\dot{\bar{\gamma}}_{\kappa}^{\varphi} \quad \text{Eq. (A4c)}$$

where $\boldsymbol{\sigma}$ is the Cauchy stress tensor, and $h^{\alpha\vartheta}$ and $h_k^{\beta\varphi}$ are the hardening moduli of the parent and child respectively. A power-law relationship is used to capture the combined effects of work hardening and recovery:

$$h^{\alpha\vartheta} = \begin{cases} h_0^{\vartheta}\left[1 - \dfrac{s^{\vartheta}}{s_s^{\vartheta}}\right]^{a^{\vartheta}} & \text{if} \quad \alpha = \vartheta \text{ (coplanar systems)} \\ h_0^{\vartheta} q\left[1 - \dfrac{s^{\vartheta}}{s_s^{\vartheta}}\right]^{a^{\vartheta}} & \text{if} \quad \alpha \neq \vartheta \end{cases} \quad \text{Eq. (A5)}$$

where q is the latent hardening ratio, h_0^{ϑ} denotes the initial hardening parameter, s_s^{ϑ} is the saturation slip resistance, and a^{ϑ} is a material constant that controls the sensitivity of the hardening moduli to the slip resistance.

The homogenized response of a material point can be obtained using the Taylor-law as follows:

$$\boldsymbol{\sigma} = (1 - f_{tw})\boldsymbol{\sigma}^{mt} + \sum_{k=1}^{n_t^{mt}} f_{tw}^{k}\boldsymbol{\sigma}_k^{tw} \quad \text{Eq. (A6)}$$

where f_{tw} is the total fraction of the reoriented children nucleated due twinning, i.e., $f_{tw} = \sum_{\kappa=1}^{n_t^{mt}} f_{tw}^{k}$, f_{tw}^{k} is the fraction of the reoriented child nucleated due to the activation of k^{th} twin system of the parent, and n_t^{mt} is the number of nucleated children.

In the current work, the sample was loaded in uniaxial compression and no detwinning occurred. Accordingly, the original twinning-detwinning model of Yaghoobi et al. [24] was simplified. Two operations responsible for twinning are considered, termed operations *A* and *B*. The twin can grow due to the parent reduction which occurs when $\tau^{N_s^{mt}+k} > s^{N_s^{mt}+k}$ (Operation A). A twin can also grow due to the child propagation which occurs when $\tau_k^{N_s^{tw}+2} < 0$ and $\left|\tau_k^{N_s^{tw}+2}\right| > s_k^{N_s^{tw}+2}$ (operation *B*). Accordingly, the evolution of twin fraction is defined as follows:

$$\dot{f}_{tw}^{\kappa*} = [1 - f_{tw}]\frac{\dot{\gamma}^{N_s^{mt}+k}}{S} + f_{tw}^{\kappa}\frac{\dot{\bar{\gamma}}_k^{N_t^{tw}+2}}{S} \quad \text{Eq. (A7)}$$

where S is the characteristic twin shear strain, which is calculated as 0.129 in the case of magnesium [47], $\dot{\gamma}^{N_s^{mt}+k}$ is the shear rate of $(N_s^{mt}+k)^{th}$ system inside the parent corresponds to operation A, and $\dot{\bar{\gamma}}_k^{N_s^{tw}+2}$ is the shear rates of $(N_{tw}^{s}+2)^{th}$ systems inside the child nucleated due to the activation of k^{th} twin system of the parent, which corresponds to operations B. In this model, after the twin fraction of $f_{tw}^{\kappa*}$ reaches a critical value of f_0, the child is created by lattice reorientation of parent according to the κ^{th} twin system, and $\dot{f}_{tw}^{\kappa}$ and f_{tw}^{κ} become equal to $\dot{f}_{tw}^{\kappa*}$ and $f_{tw}^{\kappa*}$.

The evolution of total nucleated children fraction f_{tw} is defined as:

$$\dot{f}_{tw} = \sum_{k=1}^{n_t^{mt}} \dot{f}_{tw}^{k} \quad \text{Eq. (A8)}$$

where n_t^{mt} is the number of children nucleated due to twinning with a twin volume fraction larger than f_0. Here, as the full scale CPFE is conducted, compared to the work of Yaghoobi et al. [24] in which each grain was modeled using a cube element, multiple twin reorientation is prohibited. After one twin system reaches a critical orientation threshold of f_0, other twin systems are deactivated at that material point.

Appendix B. Calculation of the Strain Accommodation Parameters

This section describes the calculation of the strain accommodation parameters, using a similar approach to Reference [12,13,17]. Briefly, the deformation gradient tensor of the considered twin system was expressed in the reference frame of a neighboring grain, and the transformed displacement gradient tensor was taken to represent the extent of deformation needed in the neighboring grain to accommodate the considered twinning. The analysis involves tensor transformation in multiple sets of coordinate systems: (1) the twinning coordinates in the parent grain (T^P), (2) the crystal coordinates of the parent grain (C^P), (3) the lab coordinates (C^L), (4) the crystal coordinate of the neighboring grain (C^N), and (5) the slip or twinning coordinates in the neighboring grain (T^N).

For the slip or twinning system coordinate (T^P and T^N), the **x** direction corresponds to the slip/shear direction, the **z** direction corresponds to the slip/twinning plane normal, and the **y** direction is perpendicular to the **z**-**x** plane following the right-hand rule, which is the shear plane normal for a twinning system. The displacement gradient tensor (**E**) of twinning can be defined in the twinning coordinates of the parent grain by the following equation, where γ is the twinning shear with value 0.129:

$$\mathbf{E}^{T^P} = e_{ij} = \begin{pmatrix} e_{xx} & e_{xy} & e_{xz} \\ e_{yx} & e_{yy} & e_{yz} \\ e_{zx} & e_{zy} & e_{zz} \end{pmatrix} = \frac{\partial \mathbf{u}}{\partial \mathbf{x}} = \begin{pmatrix} \frac{\partial u}{\partial x} & \frac{\partial u}{\partial y} & \frac{\partial u}{\partial z} \\ \frac{\partial v}{\partial x} & \frac{\partial v}{\partial y} & \frac{\partial v}{\partial z} \\ \frac{\partial w}{\partial x} & \frac{\partial w}{\partial y} & \frac{\partial w}{\partial z} \end{pmatrix} = \begin{pmatrix} 0 & 0 & \gamma \\ 0 & 0 & 0 \\ 0 & 0 & 0 \end{pmatrix} \quad \text{Eq. (B1)}$$

Based on the orientation relationship between different coordinate systems, the displacement gradient tensor $\mathbf{E}^{T^P}$ can be transformed and expressed in any of the five coordinate systems introduced previously, following the path: $T^P \rightarrow C^P \rightarrow C^L \rightarrow C^N \rightarrow T^N$.

The tensor transformation was performed from T^P to T^N, following the method described by Shi et al. [17], which extended prior works [12,13] by considering crystal symmetry. For each twin system under consideration, the displacement gradient tensor was transformed into the coordinates of all possible slip and twinning systems (including all possible variants) in the neighboring grain, which were considered as the accommodation deformation modes. 24 slip or twinning systems belonging to 5 deformation modes were analyzed, including 3 variants of basal slip, 3 variants of prismatic slip, 6 variants of pyramidal <*a*> slip, 6 variants of 2nd order pyramidal <*c*+*a*> slip, and 6 variants of extension twinning. The transformed displacement gradient tensor was expressed in the *i*th ($i = 1, 2, \ldots 24$) accommodation deformation mode in the neighboring grain as:

$$\mathbf{E}^i = \begin{pmatrix} e^i_{xx} & e^i_{xy} & e^i_{xz} \\ e^i_{yx} & e^i_{yy} & e^i_{yz} \\ e^i_{zx} & e^i_{zy} & e^i_{zz} \end{pmatrix} \quad \text{Eq. (B2)}$$

A physical meaning was associated with the e^i_{xz} component, as it represents the shear along the accommodating slip/twin direction, on the accommodating slip/twin plane. The maximum e^i_{xz} of all the variants of the same accommodation deformation mode, here denoted as e^M_{xz} (M = one of the 5 deformation modes), was used to represent the accommodation that needs to be provided by the deformation mode in the neighboring grain.

Shi et al. [17] introduced two parameters in the range [0, 1], defined as follows, to evaluate the extent of high demand and low demand of the accommodation deformation modes:

$$\gamma^M = \frac{e^M_{xz}}{max\left(e^M_{xz}\right)}; \quad \varepsilon^M = \frac{min\left(e^M_{xz}\right)}{e^M_{xz}} \quad \text{Eq. (B3)}$$

A preferred distribution of the two parameters were found for active low SF twin variants in their study. For example, the active twin variants tend to require the most/more accommodation in the neighboring grain through basal slip (large γ^{basal}), and the least/less accommodation through pyramidal slip (large ε^{prism}).

References

[1] B.L. Mordike, T. Ebert, Magnesium Properties - applications - potential, Mater. Sci. Eng. 302 (2001) 37–45, https://doi.org/10.1016/S0921-5093(00)01351-4.

[2] A.A. Luo, Recent magnesium alloy development for elevated temperature applications, Int. Mater. Rev. 49 (2004) 13–30, https://doi.org/10.1179/095066004225010497.

[3] I.J. Beyerlein, M. Arul Kumar, The stochastic nature of deformation twinning: application to HCP materials, Handb. Mater. Model. (2018), https://doi.org/10.1007/978-3-319-42913-7_103-1, 1–39.

[4] L. Capolungo, I.J. Beyerlein, Nucleation and stability of twins in hcp metals, Phys. Rev. B Condens. Matter 78 (2008), 024117, https://doi.org/10.1103/PhysRevB.78.024117.

[5] I.J. Beyerlein, R.J. McCabe, C.N. Tomé, Effect of microstructure on the nucleation of deformation twins in polycrystalline high-purity magnesium: a multi-scale modeling study, J. Mech. Phys. Solid. 59 (2011) 988–1003, https://doi.org/10.1016/j.jmps.2011.02.007.

[6] C.D. Barrett, H. El Kadiri, The roles of grain boundary dislocations and disclinations in the nucleation of {1 0 1 2} twinning, Acta Mater. 63 (2014) 1–15, https://doi.org/10.1016/j.actamat.2013.09.012.

[7] S.J. Zheng, I.J. Beyerlein, J. Wang, J.S. Carpenter, W.Z. Han, N.A. Mara, Deformation twinning mechanisms from bimetal interfaces as revealed by in situ straining in the TEM, Acta Mater. 60 (2012) 5858–5866, https://doi.org/10.1016/j.actamat.2012.07.027.

[8] J. Wang, J.P. Hirth, C.N. Tomé, (-1 0 1 2) Twinning nucleation mechanisms in hexagonal-close-packed crystals, Acta Mater. 57 (2009) 5521–5530, https://doi.org/10.1016/j.actamat.2009.07.047.

[9] I.J. Beyerlein, C.N. Tomé, A probabilistic twin nucleation model for HCP polycrystalline metals, Proc. R. Soc. A Math. Phys. Eng. Sci. 466 (2010) 2517–2544, https://doi.org/10.1098/rspa.2009.0661.

[10] I.J. Beyerlein, L. Capolungo, P.E. Marshall, R.J. McCabe, C.N. Tome, Statistical analyses of deformation twinning in magnesium, Philos. Mag. A 90 (2010) 2161–2190, https://doi.org/10.1080/14786431003630835.

[11] É. Martin, L. Capolungo, L. Jiang, J.J. Jonas, Variant selection during secondary twinning in Mg-3%Al, Acta Mater. 58 (2010) 3970–3983, https://doi.org/10.1016/j.actamat.2010.03.027.

[12] J.J. Jonas, S. Mu, T. Al-Samman, G. Gottstein, L. Jiang, E. Martin, The role of strain accommodation during the variant selection of primary twins in magnesium, Acta Mater. 59 (2011) 2046–2056, https://doi.org/10.1016/j.actamat.2010.12.005.

[13] S. Mu, J.J. Jonas, G. Gottstein, Variant selection of primary, secondary and tertiary twins in a deformed Mg alloy, Acta Mater. 60 (2012) 2043–2053, https://doi.org/10.1016/j.actamat.2012.01.014.

[14] G. Liu, R. Xin, X. Shu, C. Wang, Q. Liu, The mechanism of twinning activation and variant selection in magnesium alloys dominated by slip deformation, J. Alloys Compd. 687 (2016) 352–359, https://doi.org/10.1016/j.jallcom.2016.06.136.

[15] D. Guan, B. Wynne, J. Gao, Y. Huang, W.M. Rainforth, Basal slip mediated tension twin variant selection in magnesium WE43 alloy, Acta Mater. 170 (2019) 1–14, https://doi.org/10.1016/j.actamat.2019.03.018.

[16] M. Yaghoobi, Z. Chen, A.D. Murphy-Leonard, V. Sundararaghavan, S. Daly, J. E. Allison, Deformation twinning and detwinning in extruded Mg-4Al: in-situ experiment and crystal plasticity simulation, Int. J. Plast. 155 (2022), 103345, https://doi.org/10.1016/j.ijplas.2022.103345.
[17] Z.Z. Shi, Y. Zhang, F. Wagner, P.A. Juan, S. Berbenni, L. Capolungo, J.S. Lecomte, T. Richeton, On the selection of extension twin variants with low Schmid factors in a deformed Mg alloy, Acta Mater. 83 (2015) 17–28, https://doi.org/10.1016/j.actamat.2014.10.004.
[18] L. Zhao, B. Guan, Y. Xin, X. Huang, C. Liu, P. Wu, Q. Liu, A quantitative study on mechanical behavior of Mg alloys with bimodal texture components, Acta Mater. 214 (2021), https://doi.org/10.1016/j.actamat.2021.117013.
[19] J. Luster, M.A. Morris, Compatibility of deformation in two-phase Ti-Al alloys: dependence on microstructure and orientation relationships, Metall. Mater. Trans. 26 (1995) 1745–1756, https://doi.org/10.1007/BF02670762.
[20] L. Wang, Y. Yang, P. Eisenlohr, T.R. Bieler, M.A. Crimp, D.E. Mason, Twin nucleation by slip transfer across grain boundaries in commercial purity titanium, Metall. Mater. Trans. 41 (2010) 421–430, https://doi.org/10.1007/s11661-009-0097-6.
[21] W.Z. Abuzaid, M.D. Sangid, J.D. Carroll, H. Sehitoglu, J. Lambros, Slip transfer and plastic strain accumulation across grain boundaries in Hastelloy X, J. Mech. Phys. Solid. 60 (2012) 1201–1220, https://doi.org/10.1016/j.jmps.2012.02.001.
[22] P.V. Houtte, Simulation of the rolling and shear texture of brass by the Taylor theory adapted for mechanical twinning, Acta Metall. 26 (1978) 591–604, https://doi.org/10.1016/0001-6160(78)90111-6.
[23] C.N. Tomé, R.A. Lebensohn, U.F. Kocks, A model for texture development dominated by deformation twinning: application to zirconium alloys, Acta Metall. Mater. 39 (1991) 2667–2680, https://doi.org/10.1016/0956-7151(91)90083-D.
[24] M. Yaghoobi, J.E. Allison, V. Sundararaghavan, Multiscale modeling of twinning and detwinning behavior of HCP polycrystals, Int. J. Plast. 127 (2020), 102653, https://doi.org/10.1016/j.ijplas.2019.102653.
[25] M. Yaghoobi, G.Z. Voyiadjis, V. Sundararaghavan, Crystal plasticity simulation of magnesium and its alloys: a review of recent advances, Crystals 11 (2021), https://doi.org/10.3390/cryst11040435.
[26] S.R. Kalidindi, Incorporation of deformation twinning in crystal plasticity models, J. Mech. Phys. Solid. 46 (1998) 267–290, https://doi.org/10.1016/S0022-5096(97)00051-3.
[27] A. Staroselsky, L. Anand, A constitutive model for hcp materials deforming by slip and twinning: application to magnesium alloy AZ31B, Int. J. Plast. 19 (2003) 1843–1864, https://doi.org/10.1016/S0749-6419(03)00039-1.
[28] H. Abdolvand, M.R. Daymond, C. Mareau, Incorporation of twinning into a crystal plasticity finite element model: evolution of lattice strains and texture in Zircaloy-2, Int. J. Plast. 27 (2011) 1721–1738, https://doi.org/10.1016/j.ijplas.2011.04.005.
[29] A. Fernández, M.T. Pérez Prado, Y. Wei, A. Jérusalem, Continuum modeling of the response of a Mg alloy AZ31 rolled sheet during uniaxial deformation, Int. J. Plast. 27 (2011) 1739–1757, https://doi.org/10.1016/j.ijplas.2011.05.002.
[30] J. Zhang, S.P. Joshi, Phenomenological crystal plasticity modeling and detailed micromechanical investigations of pure magnesium, J. Mech. Phys. Solid. 60 (2012) 945–972, https://doi.org/10.1016/j.jmps.2012.01.005.
[31] A. Fernández, A. Jérusalem, I. Gutiérrez-Urrutia, M.T. Pérez-Prado, Three-dimensional investigation of grain boundary–twin interactions in a Mg AZ31 alloy by electron backscatter diffraction and continuum modeling, Acta Mater. 61 (2013) 7679–7692, https://doi.org/10.1016/j.actamat.2013.09.005.
[32] Y. Liu, Y. Wei, A polycrystal based numerical investigation on the temperature dependence of slip resistance and texture evolution in magnesium alloy AZ31B, Int. J. Plast. 55 (2014) 80–93, https://doi.org/10.1016/j.ijplas.2013.09.011.
[33] H. Qiao, M.R. Barnett, P.D. Wu, Modeling of twin formation, propagation and growth in a Mg single crystal based on crystal plasticity finite element method, Int. J. Plast. 86 (2016) 70–92, https://doi.org/10.1016/j.ijplas.2016.08.002.
[34] H. Abdolvand, M. Majkut, J. Oddershede, S. Schmidt, U. Lienert, B.J. Diak, P. J. Withers, M.R. Daymond, On the deformation twinning of Mg AZ31B: a three-dimensional synchrotron X-ray diffraction experiment and crystal plasticity finite element model, Int. J. Plast. 70 (2015) 77–97, https://doi.org/10.1016/j.ijplas.2015.03.001.
[35] D. Greeley, M. Yaghoobi, D. Pagan, V. Sundararaghavan, J. Allison, Using synchrotron radiation to improve understanding of deformation of polycrystalline metals by measuring, modelling and publishing 4D information, IOP Conf. Ser. Mater. Sci. Eng. 580 (2019), https://doi.org/10.1088/1757-899X/580/1/012017, 0–8.
[36] A. Githens, S. Ganesan, Z. Chen, J. Allison, V. Sundararaghavan, S. Daly, Characterizing microscale deformation mechanisms and macroscopic tensile properties of a high strength magnesium rare-earth alloy: a combined experimental and crystal plasticity approach, Acta Mater. 186 (2020) 77–94, https://doi.org/10.1016/j.actamat.2019.12.012.
[37] S. Ganesan, M. Yaghoobi, A. Githens, Z. Chen, S. Daly, J. Allison, V. Sundararaghavan, The effects of heat treatment on the response of WE43 Mg alloy : crystal plasticity finite element simulation and SEM-DIC experiment, Int. J. Plast. 137 (2021), 102917.
[38] M. Yaghoobi, Z. Chen, V. Sundararaghavan, S. Daly, J.E. Allison, Crystal plasticity finite element modeling of extension twinning in WE43 Mg alloys: calibration and validation, Integr. Mater. Manuf. Innov. 10 (2021) 488–507, https://doi.org/10.1007/s40192-021-00229-0.
[39] M. Yaghoobi, S. Ganesan, S. Sundar, A. Lakshmanan, S. Rudraraju, J.E. Allison, V. Sundararaghavan, PRISMS-Plasticity: an open-source crystal plasticity finite element software, Comput. Mater. Sci. 169 (2019), 109078, https://doi.org/10.1016/j.commatsci.2019.109078.
[40] Z. Chen, S. Daly, Automated identification of deformation twin systems in Mg WE43 from SEM DIC, Mater. Char. 169 (2020), 110628, https://doi.org/10.1016/j.matchar.2020.110628.
[41] A.D. Kammers, S. Daly, Self-assembled nanoparticle surface patterning for improved digital image correlation in a scanning electron microscope, Exp. Mech. 53 (2013) 1333–1341, https://doi.org/10.1007/s11340-013-9734-5.
[42] A. Githens, S. Daly, Patterning corrosion-susceptible metallic alloys for digital image correlation in a scanning electron microscope, Strain 53 (2017), e12215, https://doi.org/10.1111/str.12215.
[43] Z. Chen, W. Lenthe, J.C. Stinville, M. Echlin, T.M. Pollock, S. Daly, High-resolution deformation mapping across large fields of view using scanning electron microscopy and digital image correlation, Exp. Mech. 58 (2018) 1407–1421, https://doi.org/10.1007/s11340-018-0419-y.
[44] M.J. Marcinkowski, W.F. Tseng, Dislocation behavior at tilt boundaries of infinite extent, Metall. Trans. A 1 (1970) 3397–3401, https://doi.org/10.1007/BF03037870.
[45] H. Qiao, S.R. Agnew, P.D. Wu, Modeling twinning and detwinning behavior of Mg alloy ZK60A during monotonic and cyclic loading, Int. J. Plast. 65 (2015) 61–84, https://doi.org/10.1016/j.ijplas.2014.08.010.
[46] G.Z. Voyiadjis, M. Yaghoobi, Size Effects in Plasticity, Elsevier, 2019, https://doi.org/10.1016/C2016-0-03366-1.
[47] J.W. Christian, S. Mahajan, Deformation twinning, Prog. Mater. Sci. 39 (1995) 1–157, https://doi.org/10.1016/0079-6425(94)00007-7.